J. Membrane Biol. 133, 61–75 (1993)

The Journal of
Membrane
Biology

Exocytotic Fusion Pores Exhibit Semi-Stable States

Michael J. Curran†, Fredric S. Cohen‡, Douglas E. Chandler§, Peter J. Munson‖, and Joshua Zimmerberg†*

†Laboratory of Theoretical and Physical Biology, National Institute of Child Health and Human Development, and ‖Analytical Biostatistics Section, Division of Computer Research and Technology, National Institutes of Health, Bethesda, MD 20892, ‡Department of Physiology, Rush Medical College, Chicago, Illinois 60612, and §Department of Zoology, Arizona State University, Tempe, Arizona 85287

Summary. Rapid-freezing/freeze-fracture electron microscopy and whole-cell capacitance techniques were used to study degranulation in peritoneal mast cells of the rat and the mutant *beige* mouse. These studies allowed us to create a time-resolved picture for fusion pore formation. After stimulation, a dimple in the plasma membrane formed a small contact area with the secretory granule membrane. Within this zone of apposition no ordered proteinaceous specializations were seen. Electrophysiological technique measured a small fusion pore which widened rapidly to 1 nS. Thereafter, the fusion pore remained at semi-stable conductances between 1 and 20 nS for a wide range of times, between 10 and 15,000 msec. These conductances correspond to pore diameters 25–36 nm. Ultrastructural data confirmed small pores of hourglass morphology, composed of biological membrane coplanar with both the plasma and granular membranes. Later, the fusion pore rapidly increased in conductance, consistent with the observed morphology of omega-figures. The hallmarks of channel-like behavior, instantaneous jumps in pore conductance between defined levels, and sharp peaks in histograms of conductance dwell-time, were not seen. Since the morphology of small pores shows contiguous fracture planes, the electrical data represent pores that contain lipid. These combined morphological and electrophysiological data are consistent with a lipid/protein complex mediating both the initial and later stages of membrane fusion.

Key Words membranes · mast cells · secretion · electrophysiology · freeze-fracture · exocytosis

Introduction

Despite the privotal role membrane fusion plays in processes such as neurosecretion, fertilization, infection, inflammation, and syncytial disease, the molecular details surrounding and merging of two formerly distinct bilayer membranes are obscure. Ultrastructural studies show a small pore that connects the interior of the secretory vesicle to the extracellular milieu (Chandler & Heuser, 1980; Ornberg & Reese, 1981; Schmidt et al., 1983; Knoll, Braun & Plattner, 1991). The earliest event of exocytosis that can currently be analyzed is the electrical detection of formation and widening of smaller hydrated fusion pores (Zimmerberg et al., 1987; Breckenridge & Almers, 1987*b*; Alvarez de Toledo & Fernandez, 1988; Spruce et al., 1990; Monck et al., 1991). These pores form without osmotic stress and are reversible. The characteristics of fusion pores and their composition are of intense interest (Zimmerberg, 1987).

Various models of proteinaceous fusion pores have been proposed. In one, proteins aggregate, change conformation, and insert into membrane to form an essentially proteinaceous pore, which later widens through insertion of lipid into the channel wall (Zimmerberg, 1988; Almers, 1990). In a second model, lipids comprise the wall of the lumen of the initial fusion pore (Zimmerberg, Curran & Cohen, 1991; Oberhauser, Monck & Fernandez, 1992). Whereas the properties of many protein pores are well known from ion channel studies, the properties of pores containing lipid are completely unknown. In this study, we have measured intermediate stages of fusion during exocytosis of mast cell granules by two techniques: rapid-freezing/freeze-fracture and cell capacitance. We measured hundreds of fusion pores and examined the results statistically. Because we are studying relatively large fusion pores, it is unlikely that they are composed solely of protein. We found that these large pores, which should be rich in lipid, exhibited a preferred range of conductances. Thus, lipid-containing pores could account for the properties of initial fusion pore conductances.

* *Address for correspondence:* Bldg. 10, Room 6C101, National Institutes of Health, Bethesda, Maryland 20892, email joshz @ helix.nih.gov.

Materials and Methods

Preparation of Cells

Beige mice (C57BL/6N-bg, NIH animal facility) were sacrificed by cervical dislocation. Mast cells were obtained by peritoneal lavage with a saline solution containing (mM) 140 NaCl, 5 KCl, 1 $CaCl_2$, 1 $MgCl_2$, 5.6 glucose, and 10 HEPES, pH 7.2. Cells were attached to coverslips pretreated with 50 μg/ml poly-L-lysine (MW 300,000, Sigma, St. Louis, MO). After the cells attached, the saline solution was replaced with modified Eagle's medium (without bicarbonate) containing 10 mM HEPES, pH 7.2, and 1 mg/ml streptomycin and penicillin (ICN Biomedicals, Costa Mesa, CA). Cells were incubated at room temperature until use.

Electrical Measurements

Cell admittance was measured at room temperature by the technique of Neher and Marty (1982). Patch pipettes were pulled from Corning glass to a 2–4 MΩ resistance, coated with Sylgard (Dow, Midland, MI) and filled with an intracellular solution known to promote fusion (Fernandez, Neher, & Gomperts, 1984) composed of (mM) 150 monopotassium glutamate, 6 $MgCl_2$, 0.1 EGTA, 10 HEPES, pH 7.2, 0.5 inosine triphosphate (ITP), and 2–10 μM guanosine 5'-[3-thio]-triphosphate (GTP-γ-S). The extracellular solution was (mM) 140 NaCl, 5 KCl, 6 $CaCl_2$, 1 $mgCl_2$, 5.6 glucose, 10 HEPES, pH 7.2. Tight-seal, whole-cell recordings were obtained by standard techniques (Hamill et al., 1981). Series resistance ranged from 0.09–0.58 μS. A stimulating sine wave of 300–3,200 Hz and 100 mV peak to peak amplitude, superimposed on a holding potential of −50 mV, was applied across the cell membrane via the patch clamp (EPC-7, List Electronics, Darmstadt, Germany). The resulting current was converted to voltage by the clamp and passed to a two channel lock-in amplifier (Ortholoc 9502, Brookdeal Electronics, Bracknell, Berkshire, England), which outputs the out-of-phase (Y_{90}) and in-phase (G_{ac}) admittances. After fully compensating the whole-cell parameters, the phase was determined by nulling the response of the G_{ac} to changes in the capacitance compensation of the patch clamp, as described (Neher & Marty, 1982). This method was at worst 5% in error, and led to a 5% error in estimating pore conductances, since the pore conductance is essentially linear in the calibration factor. An alternate method for setting phase in which the response of the capacitance signal is nulled to a change in series compensation (Joshi & Fernandez, 1988), may also be used. However, there are no significant differences between the two methods for small changes in capacitance (less than 7 pF). After the phase was set, capacitance was calibrated by either a 1 or a 0.3 pF change in capacitance compensation. Phase and calibration were rechecked from each cell after each series of exocytotic events, unless the seal was disrupted (<10% of events). While changes of phase due to changes in the seal or series resistance only led to an insignificant change in the calibration of the capacitance (<10%), it may have contributed to the observation that G_{ac} did not always return to baseline.

The Y_{90} (out-of-phase, or imaginary), and G_{ac} (in-phase, or real) components were recorded directly from the lock-in amplifier, bypassing its low-pass filter, using PCM encoded magnetic tape, and a 20 kHz anti-aliasing filter.

Data Analysis

To optimize time response, recorded signals from the two-phase detector were low-pass filtered at a corner frequency of 1/4 the stimulating frequency of the sine wave V_c, with an eight-pole Bessel filter (Frequency Devices, Haverhill, MA). Changes in Y_{90} and transient changes (in G_{ac} (due to fusion) were captured with a digital oscilloscope (Nicolet, Madison, WI). Data were transferred from the oscilloscope to a microcomputer at the digitization rate of twice the filtering corner frequency. In addition, we digitally filtered the transferred data with an eight-pole Butterworth filter implemented with commercial software (MathSoft, Natick, MA). Each digitized point was considered to be a distinct measurement of admittance and was used to obtain a distinct pore conductance using original Fortran programs (obtainable upon request). In brief, these programs calculated the noise of the baseline and final Y_{90} or G_{ac} levels and rejected data that were within 2.34 standard deviations of either noise level, which gives significance at the 1% probability level using a single-tailed Gaussian distribution. We chose the first data point during the Y_{90} or G_{ac} rise (indicated by arrow in Fig. 3*E*) associated with fusion that was above the largest value of the baseline noise (*see below*) to determine the time of initiation of fusion. An alternative method, assigning the initial time to the first point 2.34 standard deviations above noise, did not change the results. Each digitized point after this initiation yielded a pore conductance.

When the pore conductance is comparable to the granule admittance (dominated by its capacitative admittance $\approx \omega C_g$), the applied sinusoidal voltage drops across both elements. Thus, the pore conductances can be detected over a range, or "window" centered around the granule admittance. That range is determined by the instrumentation noise and any fluctuations in cell capacitance. To span a larger set of pore conductances, we stimulated cells with a variety of command voltage frequencies (ω), since granule admittance is a function not only of granule size but of stimulating frequency. The experimentally controlled frequency of V_c, combined with the natural size distribution of granules, led to a large range of observed granule impedances. While for each fusion event pores were detected only within a unique window, this large range of granule admittance allowed the study to span a larger range of pore conductances than could be detected with a single stimulating frequency. To construct the dwell-time distribution for the conductance records of the observed pores, account had to be taken of this window of observable conductances for each pore (Zimmerberg, 1992). This was done by normalizing each point in the "raw" dwell-time histogram by a weight reflecting the total observation time for records (pores) which could potentially observe that particular conductance value. If such a correction were not made, spurious dwell-time peaks might arise at some conductance values simply because more "observation windows" were open at that value than at others.

The "raw" dwell-time histogram was constructed by pooling all conductance measurements for all pores, each measurement representing a discrete observation time (e.g., 1 msec). Then, the measurements were sorted in increasing order of conductance and the cumulative measurement time below each conductance computed. This cumulative function was smoothed and its first derivative computed with respect to conductance, yielding a "time-conductance density" plot or "raw" dwell-time histogram. Area under this curve represents integrated observation time of conductances in the specified conductance range.

The "corrected" dwell-time histogram was constructed by dividing values of the "raw" histogram by the appropriate obser-

vation time for each conductance value, i.e., the total length (in seconds) of records which might have produced that conductance value. The observation time ranged from about 10 sec at 0.2 nS to about 78 sec at 2 to 10 nS, descending again to 10 sec at 70 nS. To look at the subset of experiments measuring the smallest pores, we selected experiments whose observation window spanned the range of 0.2 to 2 nS.

The "modal conductance" was defined as the most frequently observed. It was computed by sorting all the conductance values observed for a particular pore, considering the sorted results as a function of time, and taking the derivative with respect to time, thereby producing the dwell-time distribution for each pore. Local maxima (modes) of this distribution should occur near conductance values at which the pore persists during its lifetime. The largest of these maxima (modes) of this distribution should occur near conductance values at which the pore predominantly persists during its lifetime. The largest mode (most persistent conductance value) is used as the modal conductance value for that pore. The histogram of modal conductance values should show peaks at those values preferred by many pores in the study.

Electron Microscopy

Peritoneal mast cells were obtained from Sprague-Dawley rats as previously described (Chandler & Heuser, 1980). Peritoneal washes from three to six rats were combined, the cells centrifuged at 200 × *g* for 5 min, the pellet washed once, and the cells resuspended in a phosphate-buffered saline (PBS) containing (mM) 150 NaCl, 4 Na_2HPO_4, 2.7 KH_2PO_4, 2.7 KCl, 1 $CaCl_2$, 5.6 glucose, 1 mg/ml bovine serum albumin, 10 U/ml heparin, pH 7.0. Just before freezing, a 0.4-ml aliquot of the stock cell suspension was centrifuged at 100 × *g* for 3 min, the supernatant removed, and the loose pellet transferred to a small square of filter paper moistened with PBS. Cells and filter paper were dipped into PBS containing 8 μg/ml of the synthetic polycation 48/80 (Sigma, St. Louis, MO), a known histamine-releasing agent. The specimen was quick-frozen (on the machine designed by Heuser et al. [1979]) by contact with a copper block cooled to 4°K with liquid helium. The samples were fractured in a Balzers 301 unit (Balzers, Nashua, NH) at −115 °C, etched for 10 sec, then replicated by deposition of platinum-carbon from an electron beam gun positioned at a 45° angle followed by carbon applied from overhead. Replicas were cleaned in sodium hypochloride and viewed at 80 kV in a Philips 300 electron microscope. Original negative magnifications were 86,000× and 130,000× as determined by calibration with a diffraction grating replica. All figures have been photographically reversed, causing platinum deposits to appear white.

Results

Membrane Contact

The initial stages of exocytosis were studied with freeze-fracture electron microscopy of rapidly frozen rat mast cells, to avoid fixation artifacts. Before being stimulated to exocytose, all mast cell granules were separated from the plasma membrane by a thin layer of cytoplasm (*see* Fig. 1*a*). In most cases this separation was 25 to 200 nm with a mean of 103 nm (n = 24), although the closest approach could be as small as 15 nm. Upon stimulation, dimple-like indentations extended inward toward the granule (arrows, Fig. 1*b–d*) formed in the plasma membrane. Stereo-paired electron micrographs confirmed that these are, in fact, invaginations of the plasma membrane (Fig. 2*a*). Indentations were usually 50–100 nm in diameter at the cell surface but were variable in depth, some being rather shallow (Fig. 1*c*) and others as deep as 100 nm or more (Fig. 1*d* and 2*a*). Occasionally, these indentations could be seen contacting the granule membrane (Fig. 1*b*). In no case, however, did the granule membrane reciprocate by deforming towards the plasma membrane.

A similar membrane deformation could be seen during fusion of adjacent granules. In Fig. 2*b* the membrane of one granule (which has presumably fused with the plasma membrane) has become distended to contact the membrane of a second granule. The contact (arrow, Fig. 2*c*) is circular, 11 nm in diameter, and appears to be crater-like in shape. The lip of the crater actually touched the protoplasmic fracture face of the granule below. The depression within the crater has been etched, suggesting that membrane fusion may have already occurred at the contact site. Membrane deformation prior to contact and fusion appeared to involve no noticeable increase or decrease in the density of intramembrane particles (Fig. 2*a*, *b*).

Pore Formation

To measure intermediates too small to detect with electron microscopy, we used the technique previously developed while testing the role of membrane swelling in fusion (Zimmerberg et al., 1987). During secretion, the large intracellular granules of beige mouse mast cells (Fig. 3*A*) fuse to the plasma membrane, leading to sequential increases in membrane surface area. When $1/\omega C_g \ll R_g$ and $R_s \ll 1/g_p + 1/\omega C_g$, as occurs in experimental practice, the full electrical equivalent circuit (Fig. 3*B*) reduces to the simplified circuit shown in Fig. 3*C*. The measured Y_{90} increases in steps (Fig. 3*D*, 5-sec time scale). Each step in Y_{90} is due to the fusion of an individual granule and the addition of its capacitance to the cell capacitance, a fact established by simultaneous electrical and video microscopy recording of the exocytotic events (Zimmerberg et al., 1987; Breckenridge & Almers, 1987*a*). A large variety in step sizes was seen (Fig. 3*D*), corresponding to the variety of granule sizes. Steps were not stereotypic, and included flickers (arrow *1*), fluctuating steps (arrow *2*), and rapid steps (arrow *3*). The dynamics

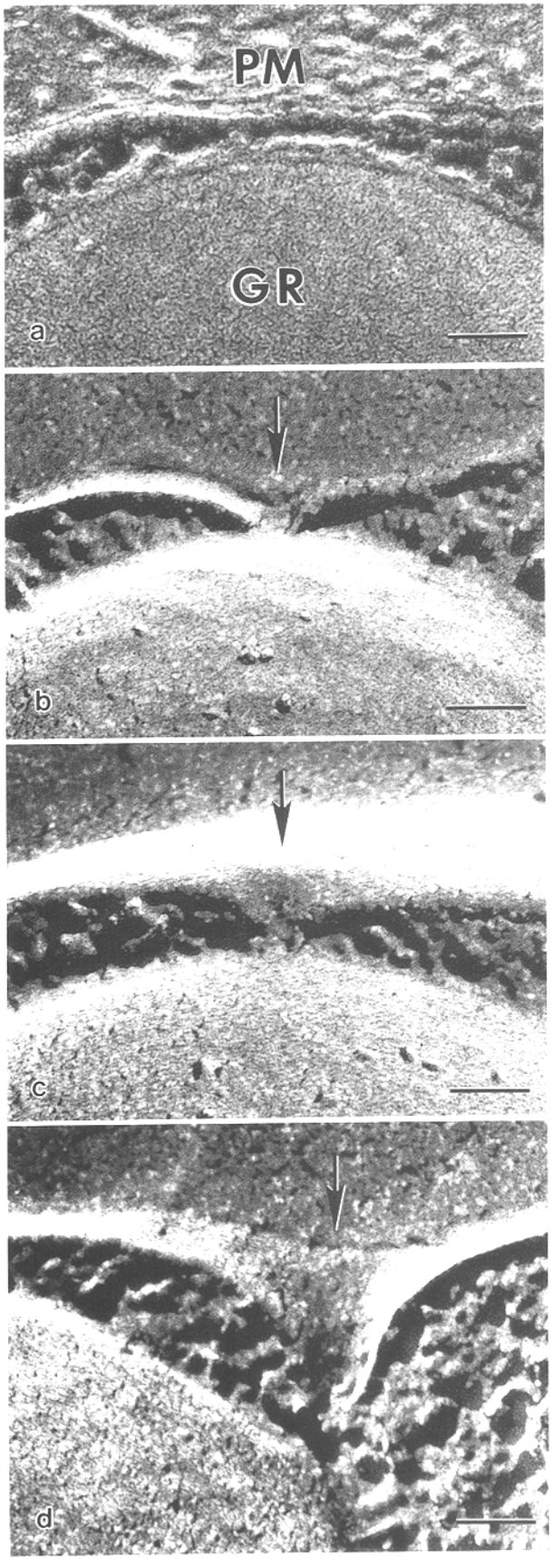

Fig. 1. Plasma-granule membrane approach prior to fusion in rat mast cells. (*a*) In unstimulated mast cells, granules (*GR*) are always separated from the plasma membrane (*PM*) by a thin layer of cytoplasm, here about 25 nm thick. The plasma membrane exhibits no indentations even at its closest point of approach to the granule membrane. (*b–d*) In cells quick-frozen 15 sec after stimulation with 8 μg/ml of the secretogogue 48/80, indentations in the plasma membrane (arrows) approach the granule membrane and in some cases appear to contact it as in (*b*). All specimens were quick-frozen, fractured, and replicated with platinum carbon. Bars = 50 nm.

of fusion pores gives rise to these variable steps in capacitance (Zimmerberg et al., 1987).

Y_{90} and G_{ac} can be measured continuously for each single fusion event (Fig. 3*E*, 10-msec time scale). As the equations used to calculate the pore conductance from Y_{90} and G_{ac} are overdetermined, the close correlation of the conductances calculated from the two components (Fig. 3*F*) provides strong evidence for the validity of the equivalent circuit used to calculate pore conductance. Single fusion events, rather than the overlap of two events involving different granules, were easily distinguished, because G_{ac} transiently rises and then returns towards baseline for each event. The expanded section in the bottom of Fig. 3*E* shows both the typical baseline noise, used to calculate error, and the time of fusion (arrow).

Time Course of Fusion Events

Fusion events were observed in 65 individual cells, with a range of 1 to 10 events per cell, for a total of 224 events. The Y_{90} increases were used to obtain the widening of the fusion pore. In seven events the steps were essentially instantaneous, i.e., the pore jump in Y_{90} to its final value of ωC_g occurred faster than the time resolution for our instrumentation (Fig. 4*A*). For the remaining 97% of the events, the pore conductance, g_p, increased during fusion in three phases, corresponding to an initial rise, an intermediate phase, and a final rapid rise in the fusion pore conductance (Fig. *4B and C*).

As measured by the discharge of the granule potential upon fusion, the fusion pore usually opens in an initial step to between 25 and 1,500 pS (Breckenridge & Almers, 1987*b*). Thereafter, the pore exhibits a variable conductance over the next millisecond, growing at a median rate of 200 pS/msec (Spruce et al., 1990). After one millisecond, the potential has discharged and pore conductance can no longer be measured by this technique. In order to measure the development of the smallest pores in beige mouse mast cells, we used a low frequency

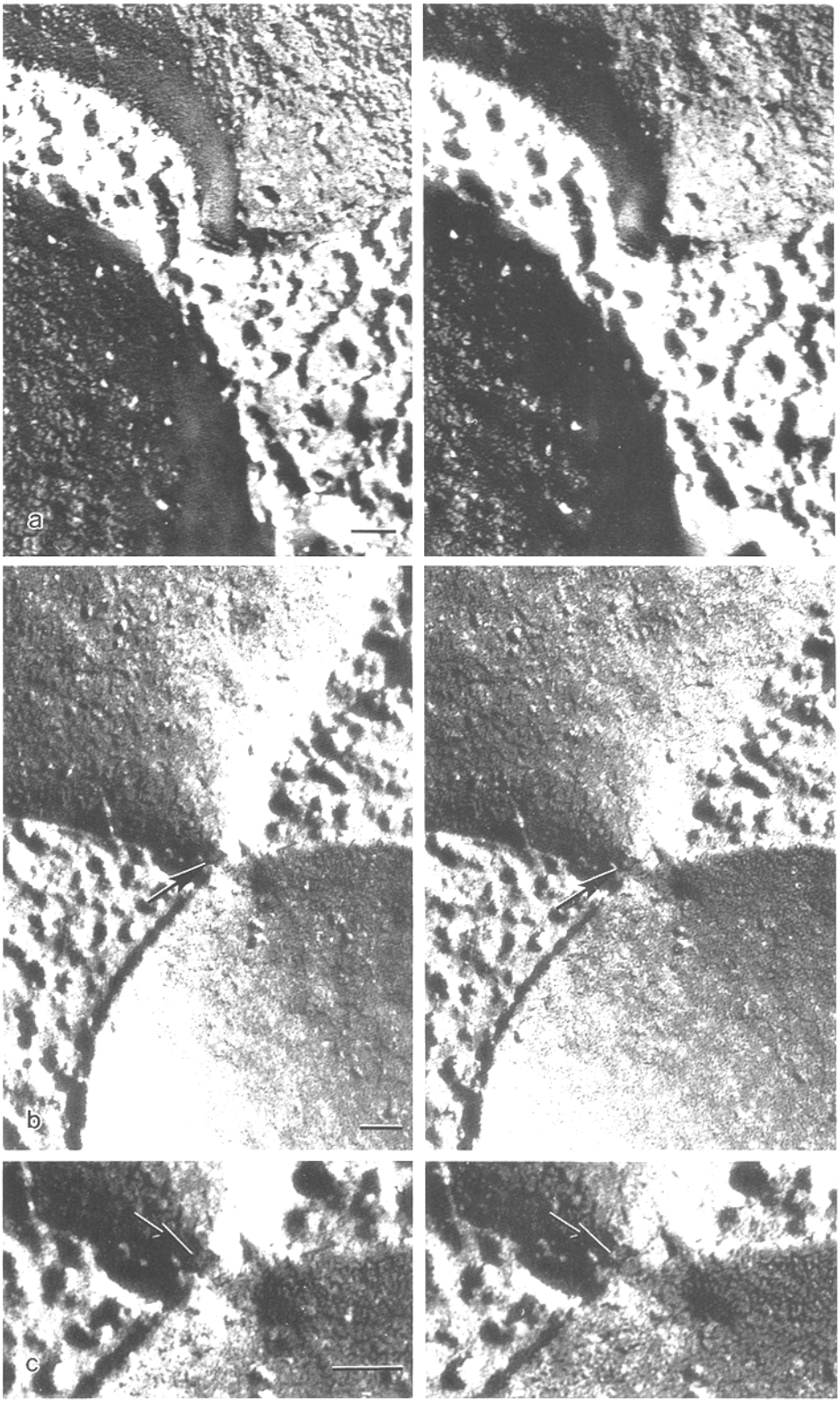

Fig. 2. Stereo-paired electron micrographs showing approach and contact of membranes during fusion. (*a*) Dimple-like indentation in the plasma membrane extends toward a secretory granule. (*b*) Two granule membranes form a highly localized contact (arrow). (*c*) The contact (arrow) is circular, 11 nm in diameter, and appears slightly etched, suggesting that fusion may have already occurred. All specimens were quick frozen 15 sec after stimulation with 48/80. Bars = 50 nm.

sine wave as the applied voltage. At low frequencies, pores are detected as soon as a few milliseconds after their formation (Fig. 4*D*). The first pore conductances we could detect were typically between about 100 and 1,000 pS, with larger conductances occurring with ever decreasing frequency (*data not*

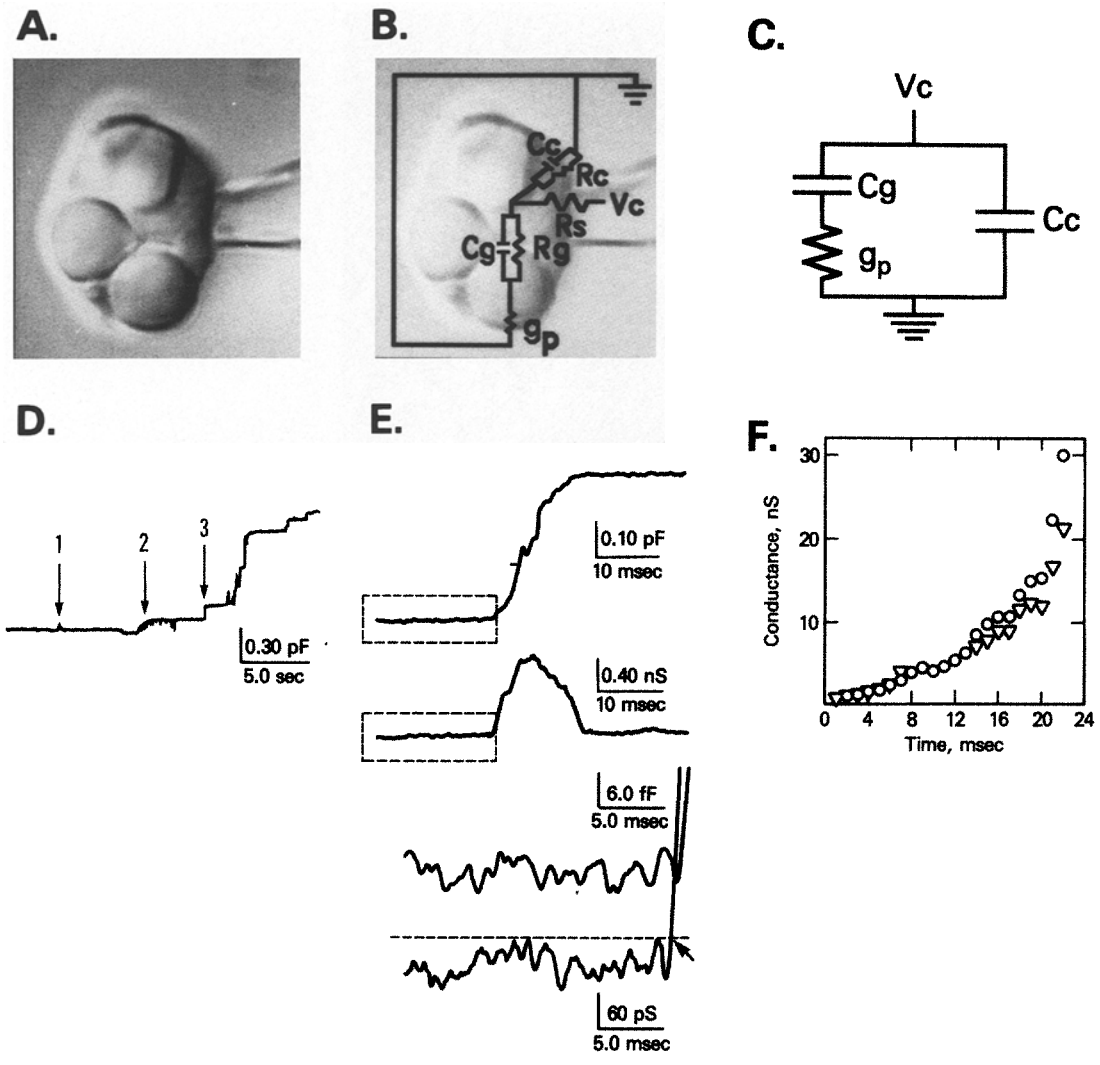

Fig. 3. A beige mouse mast cell is patch-clamped in the whole-cell recording mode (*A*). An equivalent electrical circuit representing the electrical properties of the cell during fusion of a single granule with the plasma membrane is superimposed on the cell (*B*). The equivalent circuit for the recording illustrated in (*A*) is shown superimposed on the mast cell in (*B*). The applied voltage, V_c, is applied through the pipette series resistance, R_s, and current flows to ground through either the cell membrane's capacitance, C_c, and resistance, R_c, or the granules's capacitance, C_g, and resistance, R_g. If a sine wave voltage of 300–3,200 Hz, is applied across the cell membrane, current predominantly flows through the capacitative components of the cell and granule membranes (Zimmerberg et al., 1987). Thus, the equivalent circuit reduces to a simplified circuit in (*C*), which effectively describes the time course for the conductance of an exocytotic pore. The use of this equivalent circuit allows an analytical solution for the pore conductance as a function of the measured cell admittance (1/impedance). Typical data are presented in (*D–F*). After a latency of seconds to minutes, depending upon the concentration of GTP-γ-S in the patch pipette, Y_{90} will typically increase in a stepwise fashion due to the addition of the granule capacitance (*D*). Each step corresponds to the sequential fusion of a single granule in a cell containing granules of different sizes. We examine one fusion event in detail (*E*), showing both Y_{90}, top, and G_{ac}, second from top. Expanded view of the baseline [dashed-line boxes, bottom two traces (*E*)] show the baseline noise up to the initial rise. The peak noise of the bottom trace of (*E*) is indicated by the horizontal dashed-line. The intersection of the dashed line with the data is taken as the time of fusion (arrow). Because G_{ac} is more sensitive to initial and final changes in pore conductance than Y_{90}, the first point above the baseline noise was often seen first in G_{ac}. Pore conductances were calculated from G_{ac} according to:

$$g_p(G_{ac}) = \frac{2\,G_{ac}}{1 + n\sqrt{1 - \left(\frac{2G_{ac}}{\omega c_g}\right)^2} - 2G_{ac}Rs} \qquad \begin{matrix} \text{where } n = 1,\ Y_{90} < \frac{\omega C_g}{2} \\ n = -1,\ Y_{90} < \frac{\omega C_g}{2} \end{matrix} \tag{1}$$

$$g_p(Y_{90}) = \frac{\omega C_g}{\sqrt{\frac{\omega C_g}{Y_{90}} - 1} - \omega C_g Rs} \tag{2}$$

Pore conductances are displayed in (*F*) for G_{ac} (triangles) and Y_{90} (circles).

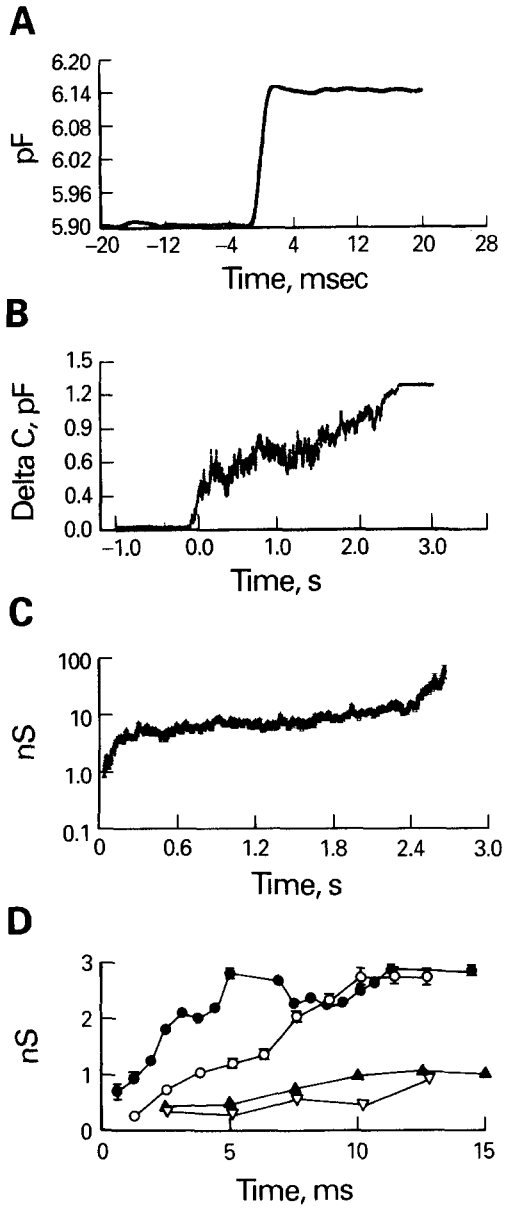

Fig. 4. The initial exocytotic fusion pore widening. Beige mouse mast cells are stimulated to degranulate while Y_{90} is recorded. (*A*) A step-increase in Y_{90} is shown. (*B*) More commonly, the increment in Y_{90} is not instantaneous, and has a fine structure. (*C*) The pore conductance of record (*B*) is calculated. Error bars in figures of individual pore conductance kinetics (shown as the thickness of the data line) show the uncertainty in pore conductance calculated from one standard deviation of the noise in the admittance baseline. Because of the transformation from admittance data to fusion pore conductance, uncertainties are not symmetric about mean pore conductances. The conductances are sometimes plotted logarithmically to show the full dynamic range of the pore size. (*D*) Initial pore conductance usually rose at greater than 100 pS/msec, but slower initial rates of increase were also observed. Different symbols refer to different experiments.

shown). The same values for early pore conductance were obtained with the two described methods of determining the first detectable pore (*see* Materials and Methods). The smallest initial pore was 158 pS from Y_{90} and 147 pS from G_{ac} (results from different experiments). Such conductances would yield inner pore diameters of 1.5 nm for pores 15 nm long, and 2.4 nm wide for pores 42 nm long, using the transform described below. This would be below the detection limit of platinum replicas produced by freeze fracture. Following detection, an initial rise in fusion pore conductance of at least 100 pS/msec over the first 10 msec was observed in 84% of the events (189/224), but initial rates were quite variable (Fig. 4*D*). The remaining events had a slower initial risetime.

Following this initial phase, the widening of the fusion pore in the intermediate phase was again variable. In some of the events, Y_{90} rose steadily to its final value (Fig. 5*A*). Equivalently, the resultant pore conductance, after the initial opening, widened monotonically upwards (Fig. 5*B*). Often the second phase of these events was characterized by random fluctuations around a rising mean (Fig. 5*C*). In other events, Y_{90} was semi-stable, i.e., hovered within a restricted range of values for a significant time (Fig. 5*D*). The resultant semi-stable pore conductance exhibited a plateau (Fig. 5*E*), shown as a mode in the dwell-time histogram of pore conductance (Fig. 5*F*).

Different subclasses of semi-stable pore conductance time courses were observed. In one subclass, the fluctuations of pore conductance during the plateau were considerable (Fig. 6*A*, *B*). This tended to occur when the mean conductance was small. In a second class of semi-stable events, the pore conductance increased in the usual manner, then decreased only to subsequently widen again (Fig. 6*C*). This was different from flicker events, defined as a pore completely closing. Conductances as small as 190 pS were seen without complete closure (Fig. 6*B*). In a third subclass, steps in pore conductance were evident (Fig. 6*E*). The dwell-time histogram for these pores showed two maxima or more (Fig. 6*F*).

The plateau phase was typically followed by a rapidly rising phase in fusion pore widening, which was irreversible (Fig. 4*C*, 5*E*). This immediately led to granular swelling.

The time course of conductance was most variable during the plateau phase. This variability was seen over a wide range of durations (1–15,000 msec), conductances (0.6–20 nS), and patterns (fluctuating *vs.* monotonically rising). The time required for the conductance to change from 0.5 to 5 nS ranged from as little as 0.6 msec to as long as 1 sec.

Distribution of Pore Conductances

To assess the temporal characteristics of pore conductances, and to search for possible semi-stable

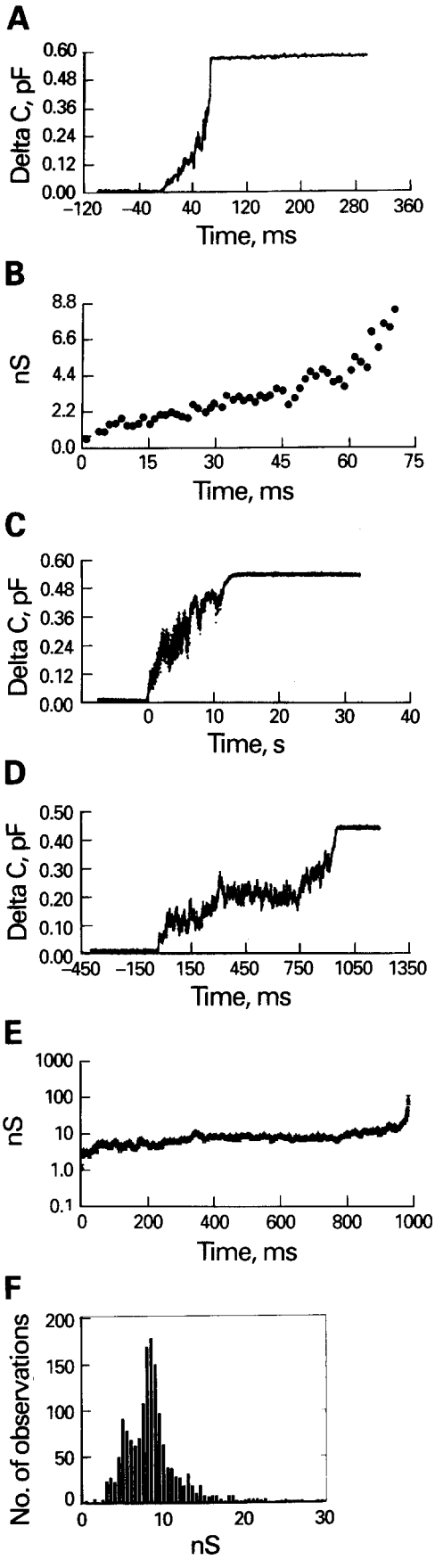

Fig. 5. When the granule in (*A*) degranulates, the Y_{90} trace shows a monotonically upwards change. The derived pore conductance shows a similar smooth rise (*B*). In other events, the Y_{90} increase is noisy (*C*), or hovers at a certain value (*D*). The derived pore conductance for (*D*) is seen in (*E*). Here, the pore conductance is stable between 6 and 10 nS for up to a second. This stability abruptly ends as pore conductance rapidly rises. A dwell-time histogram for this event is seen in (*F*) which shows two peaks, one at 6 and another at 9 nS.

conductance states, a dwell-time distribution plot was prepared. This distribution summarizes the amount of time spent at each conductance level by the entire collection of observed pores, and should reflect any tendency of pores to linger at preferred conductances (Fig. 7*A*). Because the observable range of conductances for each pore was bounded by experimental technique, and consequently more observations were made on pores within certain conductance ranges, a second distribution plot was prepared which removes this source of bias. In this distribution (Fig. 7*B*), the total observation time of pores within a particular conductance range is divided by the total time the apparatus permitted observation of this range (exposure time). Both distributions display a broad, descending peak between 0.6 and 10 nS, indicating a distinct component with a maximum at about 3–5 nS. Figure 7*B* displays a noticeable notch around 2 nS, suggesting that this value is somewhat inhibited in the data. Also, a notch would not be expected if pore conductances were simply increasing uniformly within each record. When looking with highest resolution (inset, Fig. 7*B*), both this notch and a peak at 1 nS are detected.

Because the dwell-time distribution can be influenced by a few very long-lived pores, we determined the most common, or modal conductance value for each pore, separately. As discussed above, some pores (e.g., Fig. 6*E*) showed a clear tendency to dwell at two or more distinct conductance values. However, only the modal value which persisted the longest was considered here (*see* Materials and Methods). The distribution of the modal conductance values is shown (Fig. 7*C*). The majority (78%) of pores displayed modal preferred conductance values between 1 and 5 nS. The notch at 2 nS is not seen in this model histogram.

Pore Dilation and Granular Swelling

That pore dilation occurs when granule swelling is inhibited (Monck et al., 1991) argues against the suggestion that granule swelling may influence the rate of pore dilation (Zimmerberg et al., 1987). We

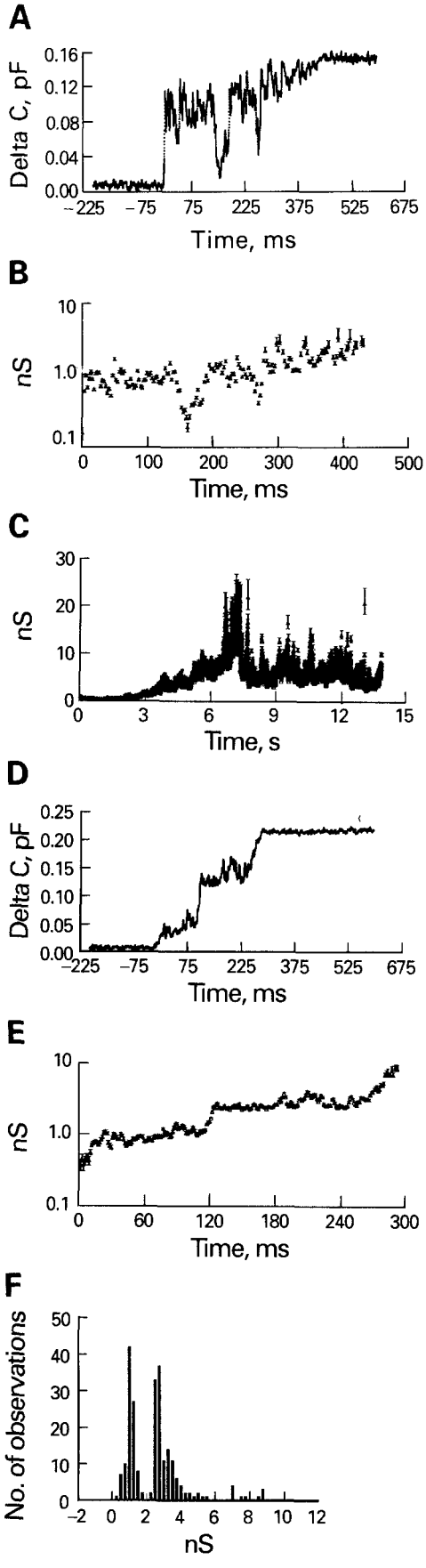

Fig. 6. Semi-stable pore conductances showing decreases and steps in conductance. (*A*, *B*) Y_{90} and calculated pore conductance for a granule in which the fusion pore closes to 190 pS before widening to finish fusion. (*C*) Calculated conductance of the longest observed pore which fluctuated between 1 and 30 nS before widening beyond detection. (*D*, *E*) Y_{90} and calculated conductance for a pore which widened in two steps. The second step did not correspond to a second granule fusing because there was no change in G_{ac}. (*F*) Dwell-time histogram for (*E*).

now report that the rapid final pore dilation was not dependent upon vesicular swelling as determined from simultaneous measurements of capacitance and vesicle morphology as previously described (Breckenridge & Almers, 1987*a*; Zimmerberg et al., 1987). The time interval between the final conductance increment for individual fusion events (from 14 vesicles in 4 cells from 3 mice) and the first detectable vesicle swelling was measured in isotonic solutions (Fig. 8). In 10 vesicles, swelling occurred 17–150 msec (i.e., 1–9 video fields, at 60 fields/sec) after the final increment in pore conductance. In three vesicles the swelling and final conductance increment occurred in the same video field, and in one vesicle the beginning of swelling occurred one field before the final conductance increment. When the experiments were repeated with solutions made hypertonic with sucrose (600 mOsm) both in the cell chamber and in the patch pipette, vesicles became flaccid (Zimmerberg et al., 1987). Under these hypertonic conditions the interval between the final conductance increment and the first detectable swelling was similar to that observed in the isotonic case. In six vesicles (from two cells from two mice) the final conductance increase was 17–300 msec before swelling, and in one vesicle the beginning of swelling occurred one field before the final conductance increment. In short, vesicle swelling neither causes nor affects any of the phases of pore dilation observed by electrophysiological methods. It does affect a further stage of pore widening observed morphologically, seen as granule discharge (Chandler, Whitaker, & Zimmerberg, 1989). However, the rapid widening of the pore detected by patch clamping may promote swelling by facilitating ion exchange (Zimmerberg et al., 1987; Curran & Brodwick, 1991).

Ultrastructure of the Exocytotic Pore

The smallest pores detected morphologically between plasma and granule membrane were variable in their dimensions. Figure 9*a* illustrates a long cylin-

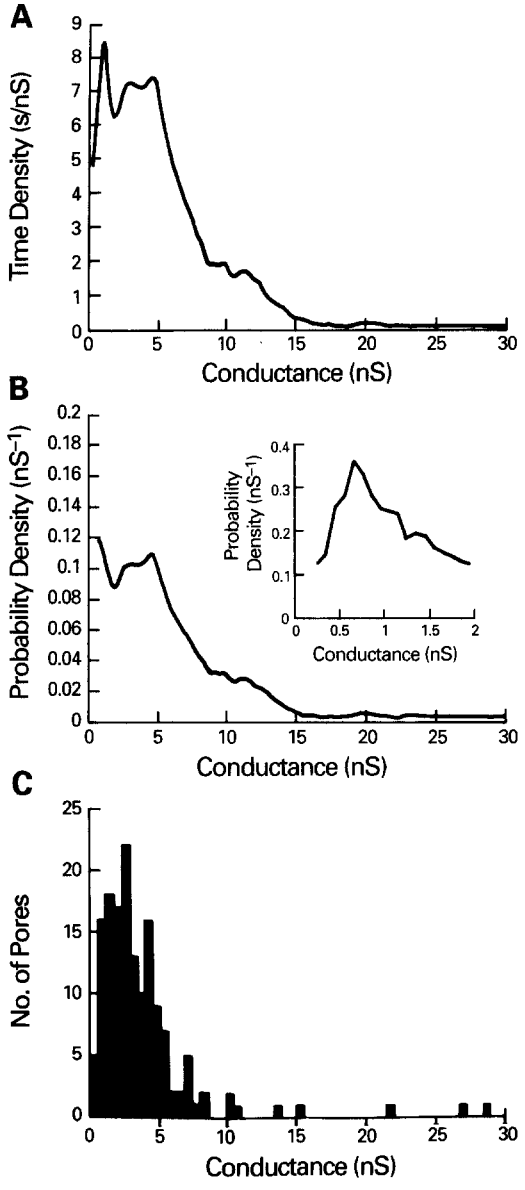

Fig. 7. Dwell-time distribution of conductance values. (*A*) Area under curve represents time spent at each range of conductance values for all pores in the collection of recordings, smoothed (program available from authors upon request). (*B*) Area under curve represents relative amount of time spent within each conductance range, adjusted for the changing total observation time for each conductance range due to the experimental conditions. The largest observation time (about 70 sec) was spent with detectability in the range 2–12 nS, so that certain regions of the distribution are de-emphasized, relative to (*A*). (*B*, inset) All records whose observation windows included the range 0.2–2 nS were selected to prepare this dwell-time histogram of the smallest pores. (*C*) Histogram of modal conductance values. For each pore (153 records), the most common (modal) conductance value attained during its observable lifetime was determined. This was accomplished by constructing the dwell-time distribution of the conductance (*see* Materials and Methods), and choosing the mode with the largest amplitude. Similar results were obtained using varying degrees of smoothing of the estimated distribution function corresponding to varying the effective bin width from 5 to 10% of the observations. The apparent second peak at 4 nS cannot be considered statistically significant.

drical pore that joined a secretory granule (*GR*) with the extracellular space (*ECS*). At this point the plasma membrane dipped inward towards the granule. The pore itself had an apparent outer diameter[1] (between arrows) of 19 nm and a length of 42 nm. This pore would have an inner diameter between 10 and 13 nm and a corresponding conductance between 2.3 and 3.6 nS. In contrast, the crossfractured, crater-like pore in Fig. 9*b* and *c* had an apparent inner diameter of 16 nm and a length no greater than its diameter. Its conductance would be 10 nS. Thus, there was considerable heterogeneity in pore diameter *and* length (*see* Fig. 10*a*). As the membrane dimples prior to fusion pore formation, the distribution of intramembrane particles in the fusion pore is similar to that of plasma or granular membrane.

Similar pores, 8 to 20 nm in diameter, were seen joining membranes of adjacent granules. Extracellular faces exhibited prominent craters (Fig. 9*d*). At high magnification the pore shown had an inner diameter of 10.5 nm (Fig. 9*e*), corresponding to a pore conductance of 3.2–6.7 nS, using a range of pore lengths from 30 to 10 nm, respectively. Likewise, depressions as small as 8 nm in diameter (arrow, Fig. 9*g*) were seen on the protoplasmic face of granule membranes (Fig. 9*f*). These could represent an early stage of pore formation although it should be cautioned that in these particular examples (Fig. 9*d–g*) we could not visualize the compartment to which these pores were joined. In most cases there was only one pore seen per contact zone, and only one contact zone seen per granule.

The histogram of pore diameters seen in freeze-fracture (Fig. 10*a*) shows that the frequency of seeing a pore is similar from 22 to 800 nm, and then decreases for larger pore diameters. The histogram of the calculated conductances of these pores (Fig. 10*b*) was based on an assumed pore length of 40 nm, and measured solution resistivity of 71 ohm-cm (Hille, 1984).

Discussion

Exocytosis in mast cells proceeds via a series of detectable steps, each with distinct kinetics: (i) The plasma membrane dimples towards the secretory granule. (ii) The two membranes adhere in a small zone of intimate contact. (iii) A small, reversible, exocytotic pore develops within this zone of apposition, allowing ion transport between the extracellu-

[1] The measured outer diameter of a pore is given by the distance between fracture planes, thought to be the dividing plane of the two lipid monolayers, plus the thickness of the platinum coating. Since Fig. 9*a* shows the E face of the fusion pore we are looking at the platinum coating the outside of the pore. The inner diameter refers to the distance between hydrated lipid head groups facing the pore aqueous interior.

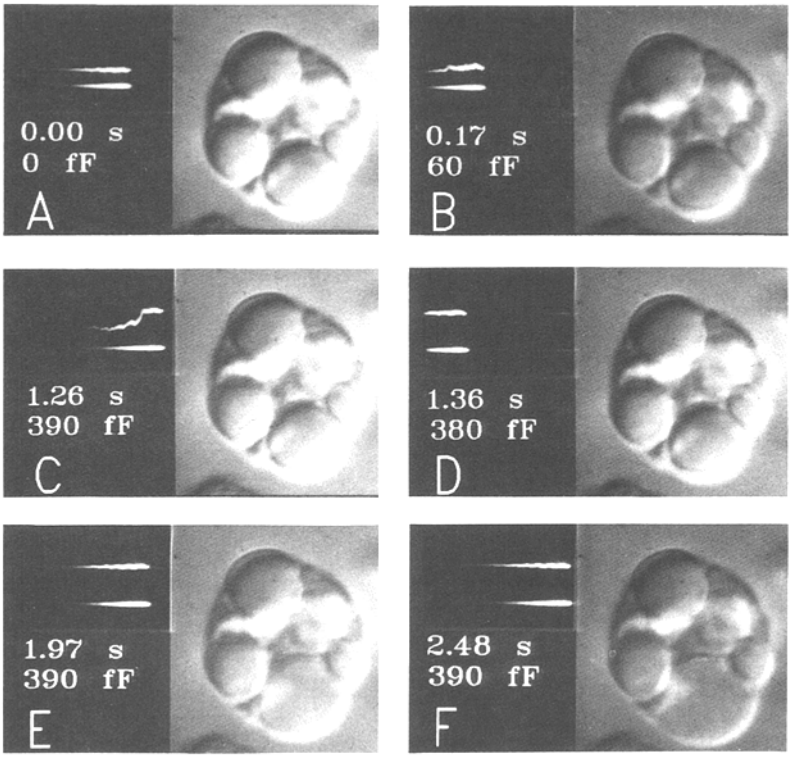

Fig. 8. Simultaneous Y_{90} and optical measurements show that the final rise in Y_{90} associated with fusion precedes the onset of vesicular swelling. Each panel, (*A–F*), arranged in chronological order, is composed of three sections; in the top left are two oscilloscope tracings, upper trace monitors Y_{90} while the lower is a reference trace; in the lower left the relative time (*s*) and relative Y_{90} (*fF*) are indicated for the image of the beige mast cell at the right. (*A*) The time and Y_{90} are arbitrarily set to zero. (*B*) Y_{90} begins to fluctuate 170 msec later (51 msec after the first change in Y_{90} above the noise). (*C*) The final change in Y_{90}. (*D*) After the final change in Y_{90} (100 msec), the first change in swelling is detectable in the vesicle at the 6 o'clock position. Because the level of detectable change is even more sensitive than the 0.18 micron resolution of the optics, the difference in vesicle size compared to that of panel (*C*) is not striking. Note that there is virtually no change in Y_{90} compared to that in panel (*C*) (The 10 fF change in Y_{90} compared to that of panel (*C*) is within the noise). (*E*) An approximate midpoint during vesicular swelling. (*F*) Completion of vesicular swelling.

lar fluid and the intragranular milieu. The conductance of this small pore rapidly expands to 0.6–1 nS. (iv) The pore conductance can be semi-stable, over a range from 0.6 to 20 nS for as long as seconds and can be viewed as an hourglass shape. (v) A rapid rise in pore conductance above 20 nS widens the pore to the next state. (vi) After pore widening, hydration of the granule contents leads to granule swelling and secretion of granule contents (Zimmerberg, 1987; Chandler et al., 1989; Merkle & Chandler, 1991).

Membrane Fusion is Preceded by a Dimple

Indentations of the plasma membrane are seen in stimulated mast cells but not in unstimulated cells. These dimples reach into the cytoplasm and in some cases are seen contacting the secretory granule below. This suggests that the site where exocytotic pore formation will occur is no larger than the tip of these dimples, an area about 50 nm in diameter. In principle, they are analogous to, although much smaller than, the plateau-like indentations of the plasma membrane seen in amoebocytes quick-frozen immediately after stimulation (Ornberg & Reese, 1981). These also serve as sites for exocytotic pore formation. Similar identations, exhibiting what may be proteinacious or lipidic particles at their tips, have been seen in the *Paramecium* plasma membrane (Knoll et al., 1991) and the sea urchin cortical granule membrane (Chandler & Heuser, 1979) although in cells treated with fixatives and glycerol. Nevertheless, growing evidence, including that in mast cells, indicates that pore formation occurs at a highly localized contact point between plasma and granule membranes.

The Exocytotic Pore Exhibits Semi-Stable States

The early stages of pore widening can be rapid or gradual, monotonic or fluctuating, whereas the late stages involve a rapid, irreversible widening. Semi-stable intermediates are found between 0.6 and 10 nS, corresponding to diameters between 4 and 22 nm. Furthermore, stepwise changes in pore conductance are occasionally seen (Fig. 6*E*). It appears that the exocytotic pore can fluctuate between semi-stable states during its expansion, exhibiting intermediate structures with measurable, although short lifetimes. This could be due to either opposing expansion and contraction forces, or to local energy minima, such that different states are within 1 kT of each other. Likely candidates for contraction forces are membrane compression and membrane curvature. Likely candidates for expansion forces are granule surface tension and hydration repulsion. It is unlikely, however, that granule matrix swelling contributes significantly to the expansion of the pore at early stages, because we

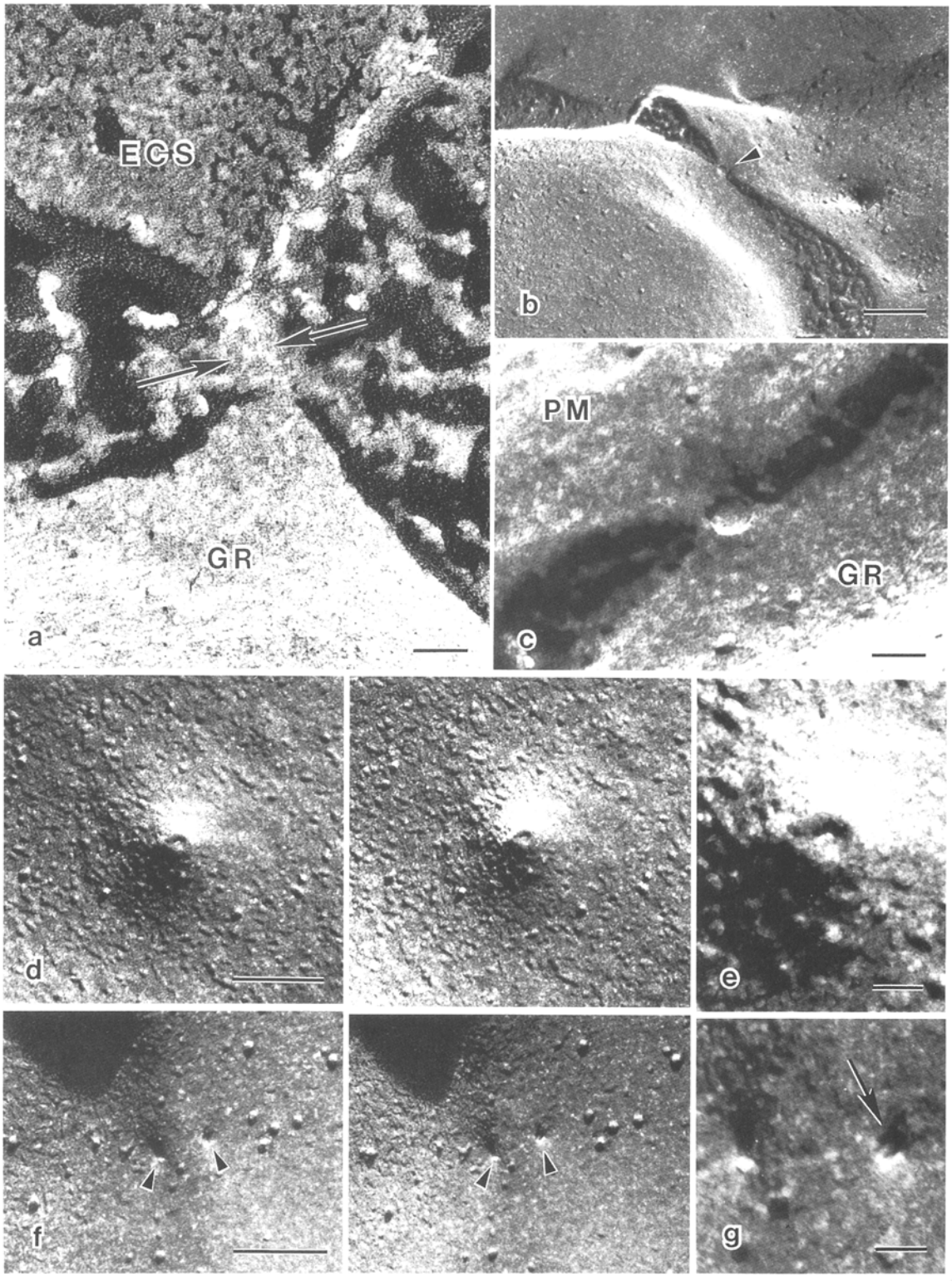

Fig. 9. Pores formed during early stages of exocytosis in rat mast cells. (*a*) A long cylindrical pore joins a secretory granule (*GR*) with the extracellular space (*ECS*). Outside diameter of the pore is 19 nm (between arrows), and its length is 42 nm. (*b*) Plasma membrane (P face) and granule membrane (E face) are joined by a small etched pore (arrow). (*c*) At higher magnification this pore has an inner diameter of 16 nm. (*d*) An etched pore on the E face of fused granule membrane stereo pair. (*e*) Inner diameter of the pore is 10.5 nm. (*f*) Small depressions on the P face of fused granule membrane that may represent points of membrane fusion: stereo pair. (*g*) The shadow within one depression (arrow) is 8 nm in diameter. All specimens were stimulated with 8 μg/ml 48/80 and quick-frozen 15 sec later. Bars = 100 nm (*b, d, and f*) or 20 nm (*a, c, e, and g*).

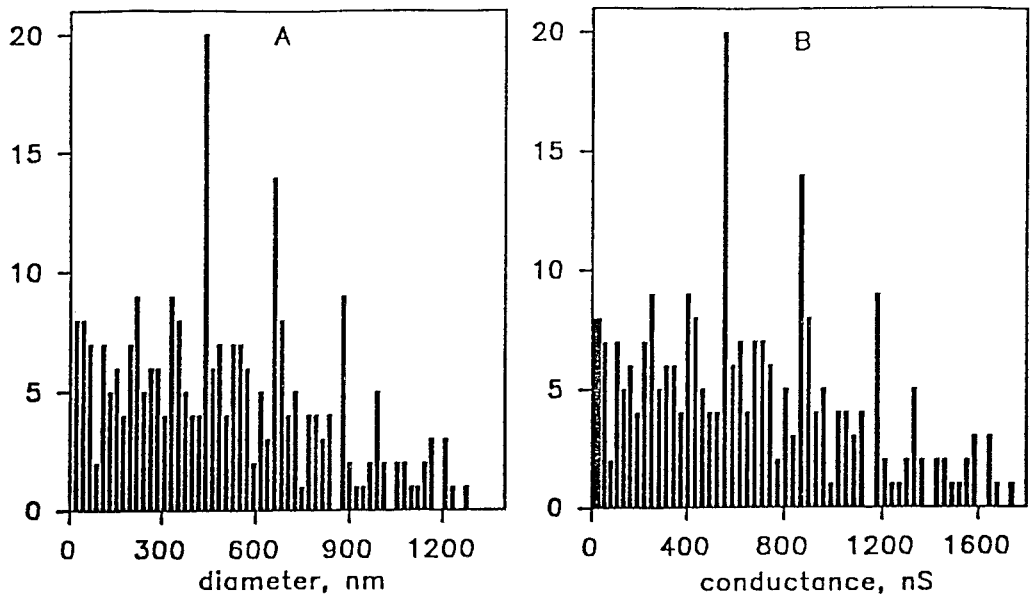

Fig. 10. (*A*) Histogram of the fusion pore diameters in rat mast cells measured from freeze-fracture data. As before, specimens were stimulated with 8 μg/ml of the secretogogue 48/80 and quick-frozen 15 sec later. Number of observations of pores with diameters between 20 and 1,300 nm are shown with intervals of 22 nm. (*B*) Histogram of the calculated conductances of pores found in freeze-fracture replicas. Calculations assume a pore length of 40 nm as described in the text.

found pore widening prior to granule swelling, and inhibition of swelling does not inhibit pore widening (Monck et al., 1991).

In view of the evidence for semi-stable states, we sought to determine whether each fusion pore exhibited preferred conductance values. For each pore, we generated a histogram of the number of times each conductance was observed (e.g., Fig. 6*F*). A smoothed version of the histogram was also obtained, in an attempt to remove "binning" artifacts (*not shown*). In some cases, pores obviously exhibited more than one"semi-stable" state (Fig. 6*F*). In an attempt to determine whether multiple semi-stable states occurred at values common to all the recorded pores, a histogram of modal conductances was analyzed. This plot (Fig. 7*C*) showed a predominant peak at around 3–5 nS, with a suggestion of a second peak at around 4 nS. The combined, corrected dwell-time histogram also showed a suggestion of multiple peaks, with the predominant one near the lower extreme of the observable range, and the suggestion of a peak between 3–5 nS (Fig. 7*B*).

Pore Dimensions

The freeze-fracture morphology of pores that have estimated conductances of 3 to 10 nS represent examples of early semi-stable states in pore growth as detected by electrophysiology. Several conclusions can be drawn from the ultrastructural appearance of these semi-stable states. First, the pore presents as an hourglass configuration and is contiguous with and joins the granule and plasma membrane. The continuous fracture plane that exists between the two fused membranes demonstrates that lipids represent a major component of the pore and are arranged in a normal bilayer configuration. Second, it is clear that there is no ordered array of intramembrane particles within or adjacent to the hourglass that would be suggestive of a wholly proteinaceous pore structure like that of a gap junction connexon. Third, the fracture faces that form the hourglass include intramembrane particles at a density not unlike that found in adjacent plasma and granule membranes. These intramembrane particles could represent protein components of a protein/lipid pore complex, although at present their identity is not known. However, not all membrane proteins fracture in such a way as to produce intramembrane particles. Thus, the pore may contain protein components that are not visualized in freeze fracture.

The values of pore conductance can be used to estimate the pore diameter (Hille, 1984). While it is possible that some matrix gel is in the lumen of the fusion pore, the measured conductivity of contracted or expanded granule matrix gel, in equilibrium with extracellular solution, was close to the conductivity of the extracellular solution itself (*data not shown*). Therefore, we use the specific conductivity of the extracellular solution for our calculation. Assuming a pore length of 1.5 to 4.2 nm as seen

in EM (Fig. 9*C*), pore conductances ranging from 0.158 to 100 nS (the range of our measurements) correspond to diameters ranging from 1.5 to 104 nm. The semi-stable intermediate pore size is between 0.6 and 20 nS, or 4.8 to 25 nm, for a pore length of 40 nm. The calculated conductances of 3, 7, and 10 nS for the pores shown in Fig. 9 have elements in the modal histogram of conductances (Fig. 7*C*). Thus, electron microscopy can detect the semi-stable states of the pore diameters seen electrically. These ultrastructural observations suggest that later stages of pore widening, between 22 and 1,300 nm, were also variable, but the frequency of seeing a pore of a given diameter is similar for most sizes (Fig. 10*A*). This suggests that the pore enlarges at a constant rate during this period.

The variable time course for the enlargement of the initial exocytotic pore implies that two pores with the same diameter, as determined by electron microscopy, need not represent equal times after fusion and could well be pores that have experienced very different life histories. Small pores, i.e., 20 nm, have also been detected with electron microscopy in amoebocytes (Ornberg & Reese, 1981), *Paramecium* (Olbricht, Plattner, & Matt, 1984) and bovine chromaffin cells (Schmidt et al., 1983). However, unlike our results that describe a broad histogram, a peak between 40–80 nm is reported for pores from the chromaffin cell. A peak in conductances corresponding to these diameters, if present, would have been detected by our technique. The apparent difference may be attributable in part to different sampling times in the kinetics of release, differences in the granule sizes, bias due to noise, or different mechanisms of fusion. For example, it is possible that the larger tension in the smaller chromaffin granule leads to a larger, semi-stable pore.

Proteins and Lipids in Pore Formation

If the incipient exocytotic pore were a stable conducting structure (like membrane protein channels and gap junctions) the decay of current resulting from the discharge of the granule membrane protential through the pore would follow a single exponential. However, the decay usually exhibits a nonexponential time course (Breckenridge & Almers, 1987*b*), suggesting that the exocytotic pore is fundamentally different from pores composed solely of protein. Also, if the exocytotic pore were composed totally of protein, the problem of merging the individual phospholipid bilayers of the granule and plasma membrane into one would remain. We have argued that lipids contribute to the initial pore (Zimmerberg et al., 1991).

When phospholipid vesicles fuse to planar phospholipid bilayer membranes, the pore conductance is greater than 10 nS within 200 μs (Cohen, Zimmerberg & Finkelstein, 1980). This suggests that the exocytotic fusion pore is not a purely lipidic structure, as has been suggested (Monck, de Toledo & Fernandez, 1990). However, both the surface tension of the bilayer and osmotic pressure of the vesicle act to rapidly widen that pore. While proteins mediate biological membrane fusion, the present study shows that the diverse initial conductances (Breckenridge & Almers, 1987*b*; Spruce et al., 1990) are naturally accounted for if the initial fusion pore is composed of a lipid/protein complex.

We would like to dedicate this paper to the memory of our friend and mentor, Alex Mauro, who emphasized to us the importance of equivalent circuits. This work was supported by National Institutes of Health grant GM-27367, and National Science Foundation grant IBN-91117509.

References

Almers, W. 1990. Exocytosis. *Annu. Rev. Physiol.* **52:**607–624

Alvarez de Toledo, G., Fernandez, J.M. 1988. The events leading to secretory granule fusion. *In:* Cell Physiology of Blood. R.B. Gunn, J.C. Parker, editors; pp. 333–334. Rockefeller University, New York

Breckenridge, L.J., Almers, W. 1987*a*. Final steps in exocytosis observed in a cell with giant secretory granules. *Proc. Natl. Acad. Sci. USA* **84:**1945–1949

Breckenridge, L.J., Almers, W. 1987*b*. Currents through the fusion pore that forms during exocytosis of a secretory vesicle. *Nature* **328:**814–817

Chandler, D.E., Heuser, J.E. 1979. Membrane fusion during secretion. Cortical granule exocytosis in sea urchins studied by quick-freezing and freeze fracture. *J. Cell Biol.* **83:**91–108

Chandler, D.E., Heuser, J.E. 1980. Arrest of membrane fusion events in mast cells by quick-freezing. *J. Cell Biol.* **86:**666–674

Chandler, D.E., Whitaker, M., Zimmerberg, J. 1989. High molecular weight polymers block cortical granule exocytosis in sea urchin eggs at the level of granule matrix disassembly. *J. Cell Biol.* **109:**1269–1278

Cohen, F.S., Zimmerberg, J.J., Finkelstein, A. 1980. Fusion of phospholipid vesicles with planar phospholipid bilayer membranes. *J. Gen. Physiol.* **75:**251–270

Curran, M.J., Brodwick, M.S. 1991. Ionic control of the size of the vesicle matrix of beige mouse mast cells. *J. Gen. Physiol.* **98(4):**771–790.

Fernandez, J.M., Neher, E., Gomperts, B.D. 1984. Capacitance measurements reveal stepwise fusion events in degranulating mast cells. *Nature* **312:**453–455

Hamill, O.P., Marty, A., Neher, E., Sakmann, B., Sigworth, F.J. 1981. Improved patch-clamp techniques for high-resolution current recording from cells and cell-free membrane patches. *Pluegers Arch.* **391:**85–100

Heuser, J.E., Reese, T.S., Dennis, M.J., Jan, Y., Jan, L., Evans, L. 1979. Synaptic vesicle exocytosis captured by quick freezing and correlated with quantal transmitter release. *J. Cell Biol.* **81:**275–300

Hille, B. 1984. Ionic Channels of Excitable Membranes. Sinauer Associates, Sunderland, MA

Joshi, C., Fernandez, J.M. 1988. Capacitance measurements: An analysis of the phase detected technique used to study exocytosis and endocytosis. *Biophys. J.* **53:**885–892

Knoll, G., Braun, C., Plattner, H. 1991. Quenched flow analysis of exocytosis in *Paramecium* cells: Time course, changes in membrane structure, and calcium requirements revealed after rapid mixing and rapid freezing of intact cells. *J. Cell Biol.* **113:**1295–1304

Merkle, C.J., Chandler, D.E. 1991. Cortical granule matrix disassembly during exocytosis in sea urchin eggs. *Dev. Biol.* **148:**429–441

Monck, J.R., de Toledo, G.A., Fernandez, J.M. 1990. Tension in secretory granule membranes causes extensive membrane transfer through the exocytotic fusion pore. *Proc. Natl. Acad. Sci. USA* **87:**7804–7808

Monck, J.R., Oberhauser, A., de Toledo, G.A., Fernandez, J.M. 1991. Is swelling of the secretory granule matrix the force that dilates the exocytotic fusion pore? *Biophys. J.* **59:**39–47

Neher, E., Marty, A. 1982. Discrete changes of cell membrane capacitance observed under conditions of enhanced secretion in bovine adrenal chromaffin cells. *Proc. Natl. Acad. Sci. USA* **79:**6712–6716

Oberhauser, A.F., Monck, J.R., Fernandez, J.M. 1992. Events leading to the opening and closing of the exocytotic fusion pore have markedly different temperature dependencies. Kinetic analysis of single fusion events in patch-clamped mouse mast cells. *Biophys. J.* **61:**800–809

Olbricht, K., Plattner, H., Matt, H. 1984. Synchronous exocytosis in *Paramecium* cells. II. Intramembranous changes analyzed by freeze fracture. *Exp. Cell Res.* **151:** 14–20

Ornberg, R.L., Reese, T.S. 1981. Beginning of exocytosis captured by rapid-freezing of *Limulus* amebocytes. *J. Cell Biol.* **90:**40–54

Schmidt, W., Patzak, W., Lingg, G., Winkler, H. 1983. Membrane events in adrenal chromaffin cells during exocytosis: a freeze-etching analysis after rapid cryofixation. *Eur. J. Cell Biol.* **32:**31–37

Spruce, A.E., Breckenridge, L.J., Lee, A.K., Almers, W. 1990. Properties of the fusion pore that forms during exocytosis of a mast cell secretory vesicle. *Neuron* **4:**643–654

Zimmerberg, J. 1987. Molecular mechanisms of membrane fusion: steps during phospholipid and exocytotic membrane fusion. *Biosci. Rep.* **7:**251–268

Zimmerberg, J. 1988. Fusion in biological and model membranes: similarities and differences. *In:* Molecular Mechanism of Membrane Fusion. S. Ohki, D. Doyle, T.D. Flanagan, S.W. Hui, and E. Mayhew, editors; pp. 181–195. Plenum, New York

Zimmerberg, J. 1993. Simultaneous electrical and optical measurements of individual membrane fusion events during exocytosis *Methods Enzymol.* **221** (*in press*).

Zimmerberg, J., Curran, M., Cohen, F.S. 1991. A lipid/protein complex hypothesis for exocytotic fusion pore formation. *Ann. NY Acad. Sci.* **635:**307–317

Zimmerberg, J., Curran, M., Cohen, F.S., Brodwick, M. 1987. Simultaneous electrical and optical measurements show that membrane fusion precedes secretory granule swelling during exocytosis of beige mouse mast cells. *Proc. Natl. Acad. Sci. USA* **84:**1585–1589

Received 31 July 1992; revised 11 November 1992